First operations with caesium of the negative ion source SPIDER

E. Sartori[1, 2], M. Agostini[1], M. Barbisan[1], M. Bigi[1], M. Boldrin[1], M. Brombin[1], R. Casagrande[1], S. Dal Bello[1], M. Dan[1], B.P. Duteil[1,3], M. Fadone[1], L. Grando[1], A. Maistrello[1], M. Pavei[1], A. Pimazzoni[1], C. Poggi[1], A. Rizzolo[1], A. Shepherd[1,4], M. Ugoletti[1], P. Veltri[5], B. Zaniol[1], R. Agnello[1,3], P. Agostinetti[1], V. Antoni[1], D. Aprile[1], V. Candeloro[1], C. Cavallini[1], R. Cavazzana[1], M. Cavenago[6], G. Chitarin[1,2], S. Cristofaro[1], M. Dalla Palma[1], R. Delogu[1], M. De Muri[1], S. Denizeau[1], F. Fellin[1], A. Ferro[1], C. Gasparrini[1], P. Jain[1], A. Luchetta[1], G. Manduchi[1], N. Marconato[1], D. Marcuzzi[1], I. Mario[1,6], R. Milazzo[1], R. Pasqualotto[1], T. Patton[1], N. Pilan[1], M. Recchia[1], A. Rigoni-Garola[1], B. Segalini[1], M. Siragusa[1], M. Spolaore[1], C. Taliercio[1], V. Toigo[1], R. Zagorski[1,7], L. Zanotto[1], M. Zaupa[1], M. Zuin[1], G. Serianni[1]

[1)] *Consorzio RFX (CNR, ENEA, INFN, Università di Padova, Acciaierie Venete SpA), Corso Stati Uniti 4, I-351, 27 Padova, Italy*
[2)] *Department of Management and Engineering, Università degli Studi di Padova, Strad. S. Nicola 3, 36100 Vicenza, Italy*
[3)] *Ecole Polytechnique Fédérale de Lausanne (EPFL) - Swiss Plasma Center (SPC), 1015 Lausanne, Switzerland*
[4)] *CCFE, Culham Science Centre, Abingdon OX14 3DB, Oxon, UK*
[5)] *ITER Organization (IO), Route de Vinon sur Verdon, CS 90 046, F-1, 3067 St. Paul-lez-Durance, France*
[6)] *Istituto Nazionale Fisica Nucleare, Italy*
[7)] *National Centre for Nuclear Research (NCBJ), PL-05-400 Otwock, Poland*

Corresponding Author: Emanuele Sartori, e-mail address: emanuele.sartori@igi.cnr.it

Abstract

The negative-ion based neutral beam injector for heating and current drive of the ITER plasma (ITER HNB) is under development, at present focusing on the optimization of the full-scale plasma source in the SPIDER test stand. The production of H^- or D^- ions in the ion source is based on the low work function surfaces obtained by caesium evaporation. This paper describes the caesium conditioning procedure and the corresponding beam performances during the first operation of SPIDER with caesium. Technical solutions to overcome present limitations of the test stand are described. The influence of source parameters on the caesium effectiveness was investigated in short beam pulse operation; with total RF power of 400 kW and filling pressure below 0.4 Pa, and a limited number of extraction apertures, a negative ion current density of about 200 A/m^2 was extracted in hydrogen, with beam energy lower than 60 keV. Beam optics and beam uniformity were assessed thanks to the acceleration of isolated ion beamlets. A possible procedure to accelerate a uniform beam was demonstrated at low RF power. The results obtained in this first investigation provided key indications on the operation of one of the largest existing sources of accelerated negative hydrogen-like ions.

Introduction

The fusion experiment ITER will deploy two neutral beam injector (NBI) systems providing heating [1,2] and current drive. The negative-ion source of each NBI shall provide a beam current of about 40 A, with a beam acceleration energy up to 1 MV for up to 3600 s. Very demanding beam parameters were defined for the two hydrogen species (roughly 285 A/m^2 of current density at the extraction and 1 MeV acceleration energy for deuterium, and 330 A/m^2 for hydrogen at a slightly lower energy of 870 keV). These target current densities are ambitious, especially with the constraint of operating the source at low filling pressure (0.3 Pa) to minimise beam losses and stray particles in the accelerator (max filling pressure 0.3 Pa).

The Radio-Frequency (RF) driven source concept for ITER NBI was developed at IPP [3], reaching maturity with the half-ITER source ELISE [4,5]. The full-scale ion source prototype SPIDER (with a size of about about 1×2 m^2 and eight RF drivers) started the operation [6,7] at the ITER neutral beam test facility [8], as an intermediate step before MITICA, the full injector prototype for ITER.

In order to achieve the required intense beam current densities, caesium vapour is injected in the plasma source, to exploit the well known mechanism [9] of negative ion production via reduction of surface work function. Many factors influence the performance of the surface production mechanism, especially in such giant negative ion sources. The effectiveness [10] of the caesium layer at the converter, i.e. the plasma-facing grid (PG), can deteriorate over time, because of a non-negligible amount of impurities contained in the background atmosphere or released from the materials exposed to the plasma. It is known that, in order to maintain the caesium effect or improve it over time, a sufficient Cs flux onto the surface shall be provided by sufficient evaporation from caesium ovens; in addition, the Cs influx should be controlled by proper management of the source wall temperatures, to guarantee ion beam stability especially during long pulses (see [11] and references therein). Alternatively, in dedicated experiments exhibiting a relatively high background pressure, it was found that the caesium layer could be reactivated by the plasma itself (by physical sputtering or chemical reduction) [12]. Controlling the Cs influx in the source is also necessary to minimise the breakdown probability in the extractor and accelerator gap [13]. Finally, spatial variations of the sheath voltage and plasma density along the very wide converter surface may determine different effective yields, due to double layer formation [14,15].

In SPIDER, caesium ovens are located on the rear part of the source, so that a large amount of the injected caesium is

received by the source backplate [16]; the caesium layer builds up at the plasma grid (PG) and bias plate (BP) both in between, and during, the plasma discharges. In the no-plasma phase, caesium reaches the PG and BP because of incomplete sticking at the surfaces where it is first deposited. In the plasma phase, caesium is desorbed from the plasma-facing elements located on the rear side of the source due to thermal evaporation or to sputtering, where plasma density and sheath potential are higher. At the PG, due to the lower plasma density, electron temperature and sheath potential, a lower desorption rate is expected for the caesium (those effects are definitely more relevant in deuterium). Having a rather high ionization probability, Cs transport towards the PG and BP is also influenced by the electric field in the plasma [17]. All these effects are intertwined, and may play a different role, depending on the plasma parameters and the history of the surfaces. The experimental investigation of caesiation procedure and of the results with surface production in the full-scale ITER source is of great interest; in the present study, the "history" effect could be neglected in the initial phases, this being the first caesiation of SPIDER that started from clean surfaces.

The results of SPIDER operation with caesium provide also another important indication regarding beam acceleration: indeed, the ITER NBI source will use a multigrid accelerator with 7 electrodes and the largest extraction area ever used for similar applications [18]. In fact, the negative ion (NI) current extracted through all apertures at any location of the plasma electrode shall be as uniform as possible, in such a way that all beamlets are as close as possible to the optimal perveance; only in this way, a complete transmission of the ion current during acceleration is possible, and the losses onto the accelerator electrodes and the beamline are minimised. Together with the optimization of the plasma uniformity in the proximity of the converter (PG), it is expected that a proper conditioning of the Cs layer could reduce the local differences from beamlet to beamlet. The Cs conditioning is a delicate phase in this sense, with the Cs layer developing sooner at certain apertures rather than others. In case of different perveances on different beamlets, operation of the multigrid accelerator is hindered. At present, the high-voltage power supply of the ITER NBI prototype MITICA allows a minimum controlled acceleration voltage of 200 kV, so that in case of beamlet growth inside the accelerator the beam particles intercepting the electrodes would have enough power for localized melting; therefore the procedure for the Cs conditioning shall be developed considering the constraints from the high-voltage accelerator. In this perspective, the investigation of the beam properties during the Cs conditioning procedure in SPIDER is very important, as the plasma source has the same dimension and extraction area as the ITER NBI.

This paper describes the experiments carried out during the first operation of SPIDER with caesium. The available SPIDER diagnostics were used to provide an insight on the caesium effect, while constantly controlling its evaporation rate. This was a first step in the exploration of the control parameters and in the definition of the procedures for the caesiation of such a large source. More importantly, the negative-ion availability over such a wide extraction surface were checked with caesium seeding, and vertical beam profiles will be discussed. The paper is organised as follows: after this introduction, section 2 describes the experimental setup and the present limits of the facility; section 3 describes the procedure used for caesiation and the effect of the main source parameters in this phase; section 4 reports the key features of the accelerated negative ion beam. The source performances, main results and open issues are summarised in section 5.

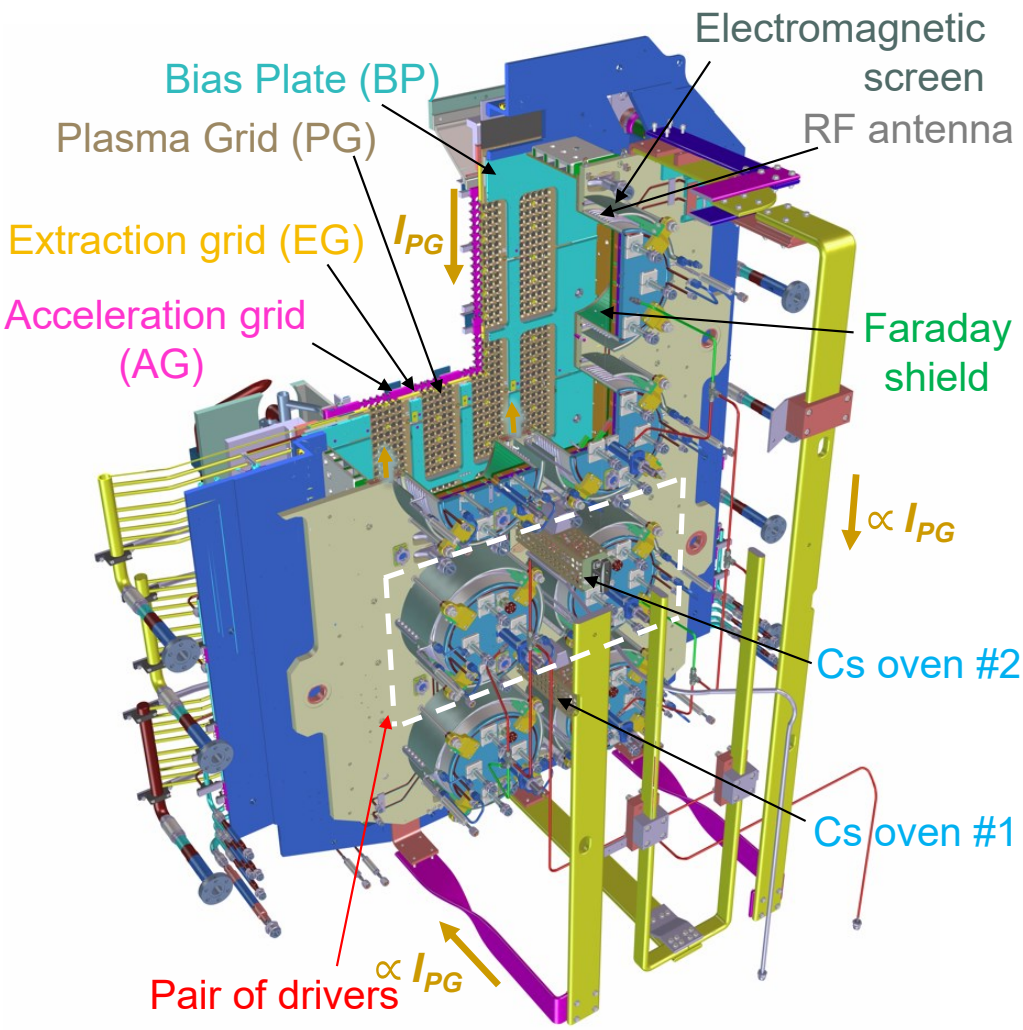

Figure 1 – Cut-out view of the main functional components of SPIDER ion source. The upper part of the plasma chamber and two pairs of drivers are shown only partially, and the caesium oven #3 at the top is not shown.

Experimental configuration of SPIDER and operation with caesium

The ion source is composed of eight cylindrical RF drivers attached to a large plasma chamber from which the negative ions are extracted (see Figure 1). The plasma, generated inside the RF drivers, expands towards the extraction electrodes through a horizontal magnetic field (recently improved [19]) – with the main purpose of reducing the electron temperature and density in favour of negative ions, thus minimising the amount of co-extracted electrons. The multi-aperture accelerator is a triode [20]. At present, the beam source is operated in pulsed mode and it is equipped with a number of beam diagnostics and source diagnostics (see [21] and references therein). The diagnostic calorimeter STRIKE [22], beam emission spectroscopy (BES) [23], optical cameras, Allison emittance scanner [24], single-beamlet current monitors (new diagnostics based on LEM sensors) provide independent measurements of the beam properties, while Langmuir probes [25], optical emission spectroscopy [26], cavity ring down spectroscopy [27], laser absorption spectroscopy [28], Langmuir-Tayor detectors [29] can provide insight on the plasma and surface processes inside the plasma source.

The horizontal magnetic field in the expansion region is created by a plasma grid-current [30] I_{PG}<5 kA flowing either upwards or downwards the plasma grid and along return bus-bars located on the rear side of the source. Such filter field was recently optimised to minimise the interference with the plasma within the drivers [19], although it still combines with the magnetic field generated by cusp magnets located both on the lateral walls and on the backplate of the drivers; an optimal interaction can be found experimentally by inverting the PG current direction. In front of the PG, the filter field strength is roughly 1.6 mT per kA of PG current; the magnetic field maps obtained from simulations were confirmed by measuring the horizontal B field strength with multiple Hall sensors at various locations inside the source [31]. In the present configuration of SPIDER, stable and reliable hydrogen plasma operation at 0.3 Pa is achieved at 50 kW/driver with a filter field strength up to 2.5~3 mT (in the vicinity of the PG). A higher filter field can be used only at higher

pressures to avoid unstable plasma discharges. At reduced power, a lower filter field must be used for a given pressure (e.g. at 23 kW/driver, it was found that the field strength cannot exceed 1.7 mT without affecting the operation of RF drivers). The RF power quoted in the present article was calibrated by inserting dual directional couplers and represents the direct power along the RF lines.

The plasma-facing electrode of the accelerator, i.e. the plasma grid, can be polarised with respect to the source and driver walls, as well as the bias plate that partially covers the plasma grid. In the IPP prototype sources, it was verified early on that controlling the bias current provides a more stable operation [3]. In SPIDER the bias plate can be independently polarised, playing a role also in the control of the co-extracted electrons [32]. The current-controlled PG and BP biases supply I^*_{bias} and I^*_{BP} respectively. A positive bias of the PG contributes to the reduction of the co-extracted electron current; the bias power supply has a 0.63 Ohm resistor in parallel [33], so that the net current from the plasma is $I_{bias} = I^*_{bias} - V_{bias}/0.63$ and $I_{BP} = I^*_{BP} - V_{BP}/0.63$. Therefore, the net current is less than the nominal one and the net collected current at the electrodes can change sign, varying roughly between -50 A and +100 A (from collecting ions to collecting electrons, respectively). At a filter field of 2.4 mT, a very reliable operation was verified in Cs-free mode at 30 kW/driver and intermediate bias currents (e.g. I^*_{bias}=80 A=I^*_{BP}).

From the thermo-mechanical point of view, the source is designed to operate in steady state. However, it was found that induced electromotive forces caused localised overheating of stainless-steel locking rings at the rear outer side of the RF drivers, producing damage and deformation. This design defect will be corrected during the next maintenance, but could not be addressed during this experimentation: the plasma duration was therefore limited to about 50 s when operating at 50 kW/driver to avoid overheating. On the other hand, geometrical improvements were implemented at the structures supporting the RF coils [40], in the attempt to reduce the breakdown probability during plasma ignition (when the loop voltages are higher).

Presently, SPIDER is equipped with 7 cryogenic pumps, totalling a nominal pumping speed of 70 m^3/s for hydrogen (the actual speed could be lower) and four turbomolecular pumps yielding an additional 8.5 m^3/s. To our knowledge, it is the first negative ion source in which the ion source was not isolated from the cryogenic pumps during regeneration, and impurities sorbed by the cryogenic system could be released to the caesiated source. In line with the expected operational mode of the ITER NBI cryogenic system, a scheme of partial regeneration has been applied throughout the experimental campaign. After every day of operation, the charcoal-coated low-temperature cryopanels, normally operating at about 10-15 K, are slowly heated while keeping a low vessel pressure of ~0.1-0.2 Pa (to avoid non-linear temperature increase of the cryopanels), so as to achieve a release of about 30 bar·L. Only in the weekends, a temperature as high as about 55-60 K could be reached, allowing the release of all stored hydrogen molecules. In this procedure, the heavier species expected to spoil the caesium layer are released only in limited amount, with also a large probability of remain trapped at the 90-110 K first stage of the cryopanels. A full regeneration of the cryopump was performed once in the last week of the campaign: however no conclusions concerning the effect on the caesium condition could be obtained, as the source performances were already decreased by the presence of an air leak (see next paragraph). In the case of 30 sec plasma pulses repeated every 3 min, the duration of gas injection per day up could reach 80 min in 8 h; at a source filling pressure of about 0.4 Pa, the cryopumps could receive up to 72 bar·L every day of operation. On the basis of the experience acquired in SPIDER on the partial regeneration procedure, it was calculated that the available time for regeneration during one week (night and weekends) would be marginally sufficient to remove the full amount of hydrogen, avoiding accumulation week after week. For these reasons, even though it would be advantageous to perform the initial phases of caesium conditioning at high filling pressure to allow high plasma density operation while limiting co-extracted electrons, the source filling pressure was limited to 0.4 Pa.

Unfortunately, the base pressure of oxygen and nitrogen in the vessel increased steadily during the campaign, due to a rather significant air leak at the large ceramic insulator of the hydraulic bushing. From the beginning to the end of the campaign, (i.e. final part of phase 3 as indicated in Figure 2) the vessel base pressure exhibited an increase by one order of magnitude from $1 \cdot 10^{-6}$ mbar to $9 \cdot 10^{-6}$ mbar, exhibiting standard air composition according to the residual gas analyser. This increase could be related to the partial regeneration procedure, which caused in the cryopumps an accumulation of atmospheric gases at the first stages; however, it is more reasonably due to an increased air leak rate (in summer, the air temperature inside the SPIDER bioshield reached 30°C, probably affecting the metal-ceramic interface at the bushing). The cause of such air leak needs to be addressed before the next experiments.

In the preceding Cs-free operation, the plasma source was routinely operated up to 400 kW nominal RF power (50 kW/driver) [7], with beam energies limited to 30 kV with the aim of understanding and minimising the influence on the plasma of the RF circuit layout and the interference among oscillators [34]. Technical solutions were applied to overcome limitations of the vacuum system and of the power supplies, thus allowing the operation while minimising the probability of RF-induced discharges on the outside of the plasma source chamber. It was found that the breakdown probability was minimised when reducing the vessel pressure below 50 mPa, so that a plasma-grid mask was applied to the downstream side of the plasma grid to limit the gas conductance of the accelerator; for a given source filling pressure, the pressure in the vessel is much reduced. This allowed also frequent beam pulses during the experimental sessions, and less frequent regeneration cycles thanks to the limited gas load to the pump [35]. The use of a very much reduced number

of beamlets was a strong limitation in terms of total accelerated current (the mask at the plasma grid covered 1252 apertures out of 1280), however it actually provided great advantages in the study of the beamlet current and optics of the single beamlets. The criteria of extracted current density can be easily verified at each beamlet with this setup. Additionally, the mask allowed the introduction of dedicated diagnostics for the single beamlets, and in general a rather effective evaluation of the uniformity of the caesium effect, thanks to a suitable distribution of isolated beamlets over the nominal cross section of the beam (1.6x0.8 m). On the other hand, in consequence of the limited number of apertures, the total extracted current is negligible and a higher equilibrium density of negative ions n_- might result before the plasma grid, with respect to a reference case with all apertures (qualitatively, in large negative ion sources, applying beam extraction reduces n_- by ~30% [36]).

The preparation of the caesium operation also included a thorough testing and qualification of the caesium ovens [37,38,39], necessary to validate the design and to quantify the evaporation rates, and also to define adequate loading procedures. Each of the three caesium ovens, fully contained inside the SPIDER vacuum vessel, was loaded with 10 g of caesium. Caesium was loaded in a glovebox in argon atmosphere; an electromagnetic valve, provided with high-temperature compatible gasket, isolates the caesium reservoir during the installation. A Taylor-Langmuir detector at the oven nozzles (or Surface Ionization Detector, SID) was used to confirm the valve aperture and to estimate the caesium evaporation rate, between plasma discharges, within ~30% accuracy [29]. In general, the correlation found between the reservoir temperature and the evaporation rate was in very good agreement with the characterization carried out in isolated experiments. For the SPIDER Cs ovens, the experimental scaling law for the evaporation rate against the vapour pressure in the reservoir (expressed in mg/h per oven) at steady-state in the absence of plasma has been found to be

$$m' \approx 13 \cdot p_{vap}(T_{res}) = 13 \cdot 10^{(5.006+4.165-3830/(273+T_{res}))} \qquad \text{eq. 1}$$

with the caesium vapour pressure in the reservoir p_{vap} being a function of the reservoir temperature T_{res} in Celsius degree. The evaporation valves are normally closed. They are opened only after the feedback-controlled reservoir temperature reaches steady state. This procedure offers considerable experimental flexibility during the operations, because the evaporation rate reaches steady-state within two minutes after the valve is opened, and the cumulated amount of Cs injected in the source can be estimated throughout the experimental campaign, within the aforementioned accuracy. The ion source walls and the plasma grid are water cooled, and their temperature - very important in determining the Cs redistribution – can be maintained to a rather steady value even during the plasma discharge. The cooling water temperature of the ion source is controlled up to 35°C, while the cooling water of the plasma grid can be preheated at a higher temperature T_{PG} up to 140°C.

As indicated in Figure 1, the SPIDER multi-aperture accelerator is a triode composed by Plasma Grid (PG), Extraction Grid (EG) and Acceleration Grid (AG or grounded grid). Negative charges are extracted from the plasma by an extraction potential U_{EG} (limited to 12 kV), and then accelerated by an additional acceleration potential U_{AG}. The installation of the acceleration power supply was only recently completed, and U_{AG} was limited to ~45 kV during the operation with caesium [40], with implications on the high-current operation as discussed later (best optics expected at U_{AG}/U_{EG} ratio of approximately 9.5). The nominal gap lengths are 6 mm between PG and EG, and 35 mm between EG and AG; the detailed geometry and their influence on the beamlet optics were discussed by Agostinetti [20]. In the absence of caesium, the vast majority of the current extracted from the source is constituted by electrons. These are dumped onto the extraction grid by electron suppression magnetic field (produced by magnets embedded in the extraction grid): the electron heat load is rather high and localised, and constitutes a serious risk for the grid from the thermomechanical point of view. The extraction voltage U_{EG} shall be chosen carefully in the transition from volume to surface production: at the beginning of caesiation it cannot be too high so as to avoid damages, and yet it should be high enough to measure the available negative ion current after the caesium effect sets in (i.e. without incurring in the Child-Langmuir limit). From numerical calculations, U_{EG} =5 kV is sufficient for NI current densities up to 130 A/m^2; on the other hand, the average power per beamlet is in the order of 400 W, below the design limit (according to experimental measurement in volume operation at 30 kW/driver and intermediate bias currents with I^*_{bias}, I^*_{BP} set to 80 A).

Finally, plasma uniformity was also considered in the definition of the initial source parameters for caesiation. As an indication for uniformity, the positive ion saturation current $I_{sat}{}^+$ from Langmuir probes embedded on the bias plate at four vertical positions wes considered: as an example, with a filter field of 2.4 mT at the plasma grid, 30 kW/driver and I^*_{bias} =80 A, the configuration with pseudo-floating bias plate (I^*_{BP} =0 A) showed an improved top-bottom uniformity, exhibiting ±27% deviation from the average (with the highest and lowest $I_{sat}{}^+$ found in correspondence of the top and bottom segment respectively).

Procedure for caesium conditioning and stable beam parameters in short-pulse operation

The initial caesium conditioning with hydrogen was investigated by repeating short pulses (or blips) of ~30-40 s at

P_{RF}=30 kW/driver, p_{fill}=0.4 Pa, U_{EG}=5 kV, U_{AG}=40 kV, I_{PG}=1.5 kA, I^*_{bias} =80 A, $I^*_{biasplate}$=0 A, T_{PG}=125°C starting from a clean source. Various pulse durations and repetition rates were studied. An initial Cs injection rate of 6 mg/h was used (2 mg/h per oven), later increased up to 24 mg/h. Each pulse was programmed as follows: a ramp of RF power is applied in the initial 10 sec; its time derivative was low in order to allow a simultaneous variation of the variable capacitor at the RF oscillators (in order to start the oscillators in controlled condition and approach the point of minimal reflected power while avoiding frequency flips [41]). The PG current and PG, BP biases were applied only after a sufficiently high RF power was reached (higher filter field strength or high bias currents could not be sustained at the very low RF power at which the pulse starts). The beam extraction starts after all parameters reach the nominal value, and continues almost until the end of the plasma. The filling pressure is measured 10-15 s after the end of the plasma discharge, in pulses with extended gas injection, purposely programmed to continue after the end of the plasma discharge. The caesium injection was never stopped during the experimental day, only closing the evaporation valve if long pauses were expected in between the plasma pulses.

An overview of the entire experimentation with caesium in SPIDER is given in Figure 2, reporting the accelerated current I_{AG} and the extraction currents I_{EG}. Note that, as shown in the figure inset, I_{EG} is defined as a total current drained form the plasma source. The five phases of the campaign are also highlighted: in phases 1 and 2, the focus was on the influence of the main parameters of caesiation; phase 3 was dedicated to the study of beam optics; during phase 4, tests for improving the voltage holding capability were performed; two experimental days were dedicated to deuterium operation, in phase 5.

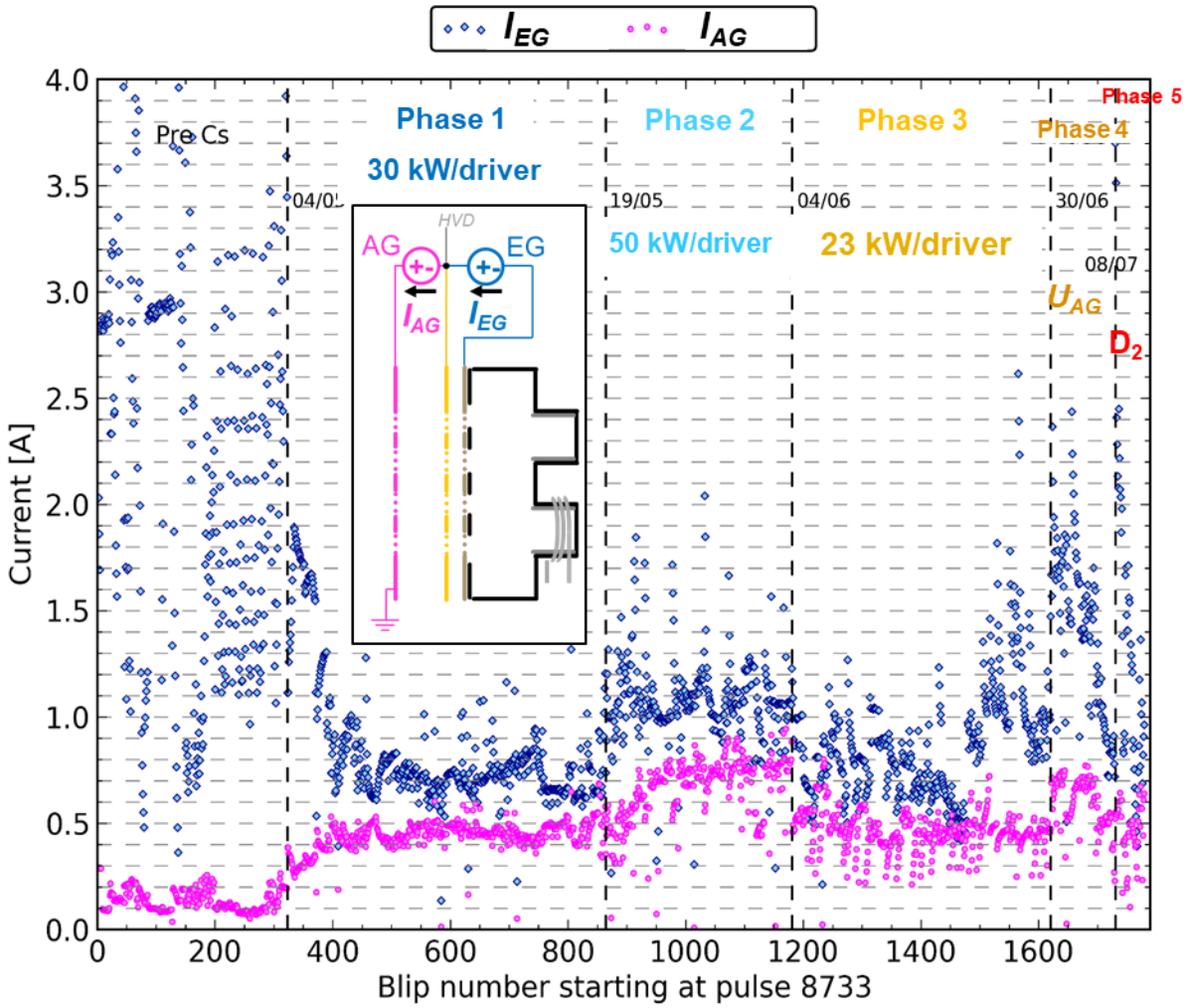

Figure 2 – Overview of the experimental campaign with caesium injection: magenta points represent the acceleration current I_{AG}, blue points indicate the extraction grid current I_{EG}, both measured at the power supplies. The five phases of the campaign are also highlighted. The currents are defined in the inset.

During the first use, the caesium reservoirs were slightly overheated, to test the Cs emission and the opening of all valves. After opening the valve with preheated reservoirs, the correct evaporation was verified using the embedded Langmuir-Taylor detectors. Plasma discharges and beam extraction could start only one hour and a half later; we estimated 12-14 mg were injected in this interval, before commencing the short pulse operation. A transition from volume to surface production was immediately seen at the first blip, with a reduction of I_{EG} from 2.4 A to about 1.0 A, and an

increase of I_{AG} by almost 400%. This would indicate a sudden decrease to electron-to-ion ratio $(I_{EG}-I_{AG})/I_{AG}$=1.5, considering the electric measurements of the power supplies.

The nominal Cs evaporation rate (eq. 1) was confirmed during operation by the Langmuir-Taylor detector embedded in the Cs ovens, which showed a saturation current $I_{SID\ bias}$ (see Figure 3(a)) coherent with the previous characterisation [38] for the different evaporation rates. The detector operated at 150 V, only in between plasma discharges, allowing to follow the stability of the evaporation or the time evolution when the reservoir temperature is changed. In addition, the Cs density inside the ion source, measured by Laser Absorption Spectroscopy 30 mm away from the PG, scales proportionally to the Cs emission rate both between plasma pulses and during plasma pulses (see figure Figure 3(b)). In general the Cs density signal at the extraction region saturates to a density of about 4-5x10^{12} m^{-3} per mg/h of evaporation (considering in particular the case of 80 °C PG temperature, as discussed later), after a minimal overshoot in the first hour after the valve is opened. Numerical models [42] indicate that this equilibrium is compatible with an average sticking probability at the ion source walls between 0.6 ~ 0.8, and would provide an average flux of approximately 3·10^{14} $m^{-2}s^{-1}$ Cs atoms to the PG per mg/h.

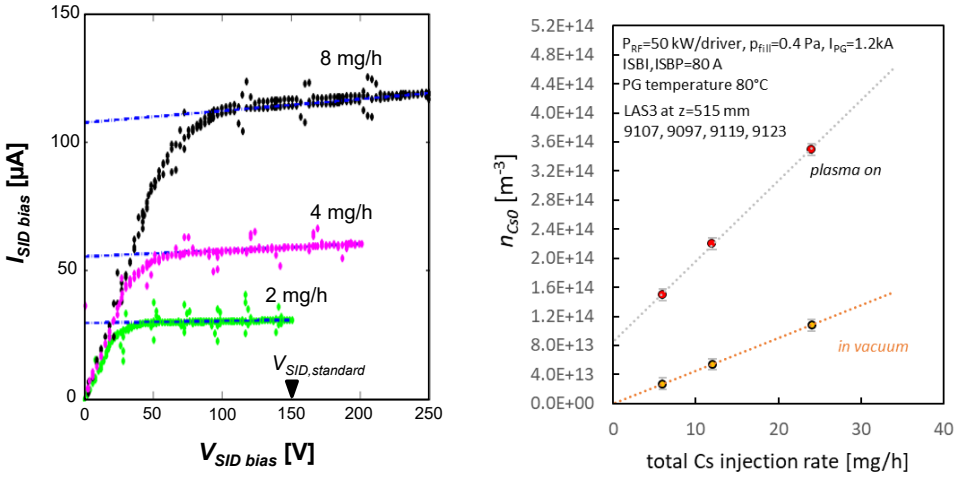

Figure 3 – (a) Current-voltage characteristics obtained between plasma pulses with the surface ionization detector embedded in each Cs oven, for three evaporation rates expressed in mg/h per oven. (b) neutral Cs density estimated via Laser Absorption spectroscopy measurements in the extraction region (at about the center of the third grid segment from the top, at a distance 30 mm from PG) as a function of the total evaporation rate from the three ovens.

Figure 4(a) exemplifies four different cases of plasma duration and repetition rate. Shorter plasma duration (27 s instead of 40s), with the same repetition time of three minutes (i.e. the time between the beginning of successive plasma pulses), gives a larger acceleration current I_{AG} and a lower extraction current I_{EG}, indicating higher NI current and lower co-extracted electron current. If the pause between the pulses is increased, i.e. repeating every 6 min instead of 3 min, I_{EG} further decreases while I_{AG} increases. Whenever the repetition rate is decreased, and the pause between plasma pulses is longer, the accelerator performances are significantly improved for the following few pulses.

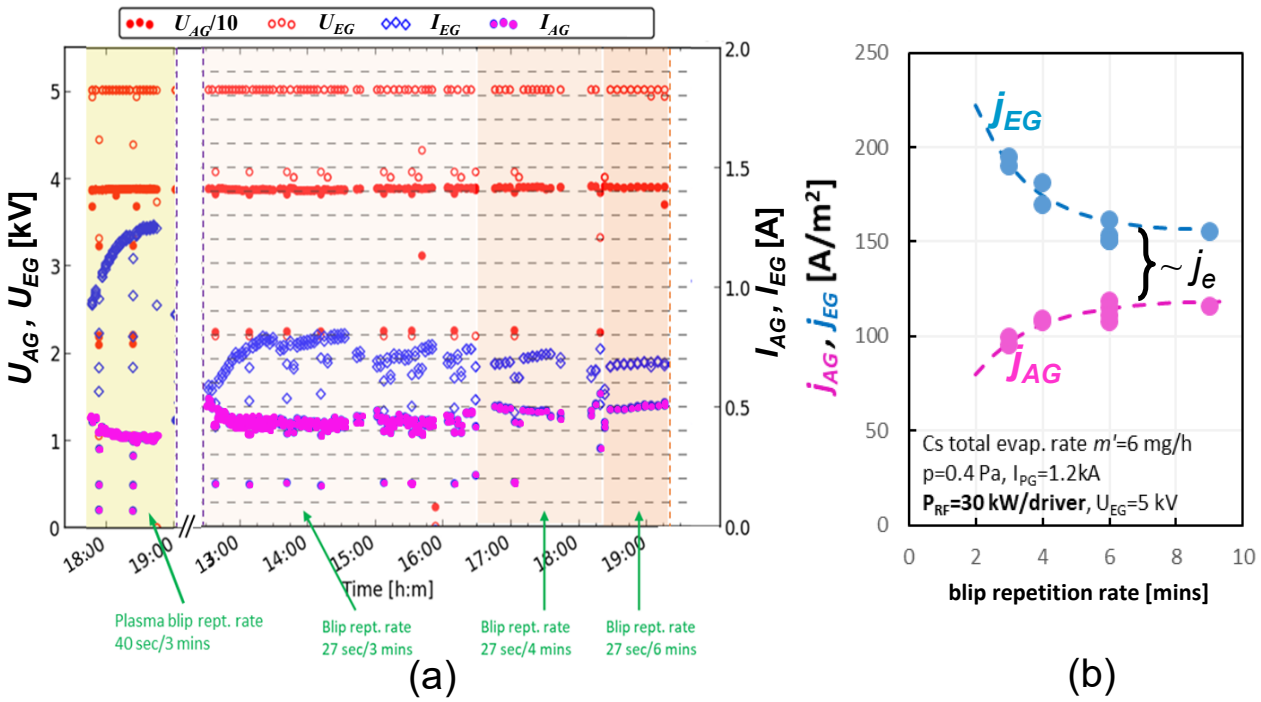

Figure 4 – On the left, I_{AG} and I_{EG} during beam pulses with different repetition rates, showing average beam parameters saturating at different values when plasma duration and repetition time between pulses are changed; on the right, saturation currents for various repetition rates.

The sequence of short pulses (or blips) was repeated until saturation of I_{AG} and I_{EG} was reached. Saturation currents are reported in Figure 4(b) with constant source parameters. I_{AG} increases with longer repetition time, similarly to the intensity of Cs 852 nm emission line in the extraction region of the plasma source (not shown; note that the quantitative relation between I_{AG} and the Cs line intensity varied with the progressing of the campaign with respect to the first days of operation).

The beam source exhibited this qualitative behaviour with the pulse repetition rate consistently throughout the campaign, independently of the total cumulated amount of evaporated caesium or the increased background gas pressure (i.e. impurities). Consequently, the effect of varying Cs evaporation rate m' on the steady-state extraction and acceleration currents can be discussed together with the pulse repetition rate t_{rept} and plasma duration t_{plasma}, as shown in Figure 5. Every point in the figure required hours of repeated pulses, before saturation was reached. In the figure, the horizontal axis is expressed as normalised duty cycle ν, calculated as

$$\nu = \frac{t_{plasma}}{t_{rept} \cdot m'} \qquad \text{eq. 2}$$

With this normalisation, an overall trend appears for both the I_{AG} and I_{EG}, within the range of parameters that were explored (13 s $< t_{plasma} <$ 40 s, 3 min $< t_{rept} <$ 9 min, 6 mg/h $< m' <$ 24 mg/h). This normalisation assumes that longer waiting time between plasma discharges at low Cs injection provides the same effect as shorter time with higher Cs injection rate. Considering the uncertainties in the measured quantities and the presence of transients in the plasma discharge, the trends appear surprisingly clear, in particular for the extracted current. Being associated to the electron current, I_{EG} is most sensitive to any variation of the caesium effect: it is expected that a lower production and extraction of NI causes a prompt increase of electron density, and in addition, small variations in the electron density can be amplified in the extracted current because of the lower mass of the electron (being inversely proportional to the square root of the mass, electrons contribution to perveance is ~ 43 times greater with respect to to H^-). The results at a RF power of 30 kW/driver during the initial phase of conditioning and the ones at 50 kW/driver are shown in the left and right hand side of Figure 5 respectively; in the higher RF power case, the extraction voltage had to be increased in such a way to overcome the Child-Langmuir limit and measure the actual NI available for extraction. In order to confirm that the chosen extraction voltage was sufficient for this purpose, in the case with highest I_{AG}, U_{EG} was raised up to 7.5 kV, registering an increase of I_{EG} below 10% and no effect on I_{AG}.

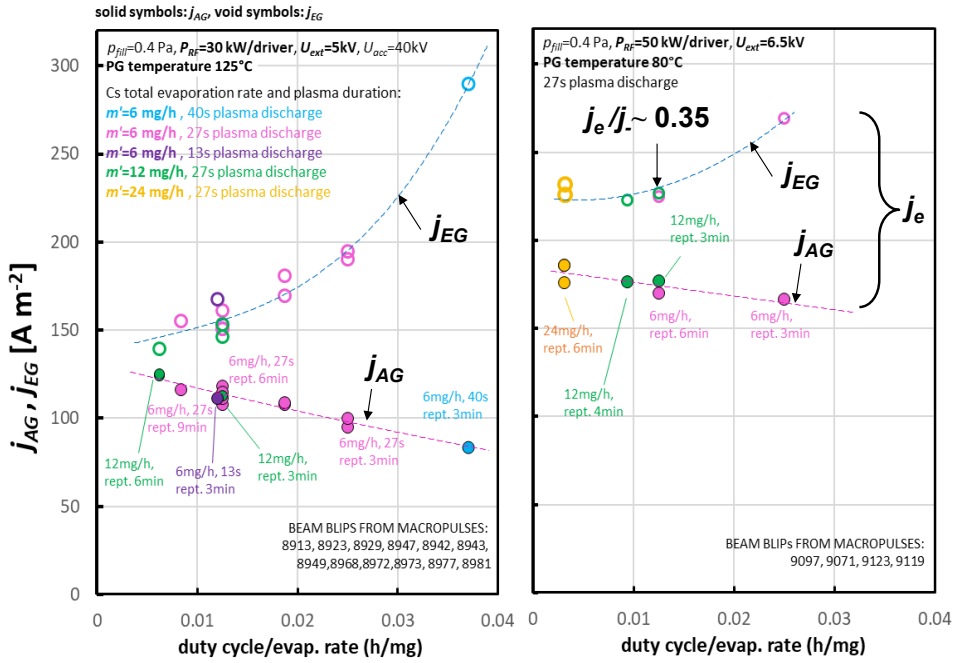

Figure 5 – Saturation values of I_{EG} and I_{AG} for various plasma duration, pulse repetition time, and caesium injection rate. On the left, RF power of 30 kW/driver; on the right 50 kW/driver. The dashed lines are just a guide for the eyes.

Figure 6 shows the influence of a fourth factor that needs to be considered, i.e. the plasma grid temperature. In SPIDER, the inlet water temperature can be controlled between 35 °C and 140 °C, with a single circuit for both plasma grid and bias plate. With the same approach of repeating short blips until a saturation is reached, the effect of PG temperature was studied within this range, identifying an influence in the rate at which the Cs layer builds up between plasma discharges. For short repetition time of 3 mins (high duty cycle), decreasing the PG temperature from 125 °C to 80 °C improved the average beam performance, with a considerable reduction of co-extracted electrons. Rather than a global improvement involving all apertures, this indicates a better development of the Cs layer at those apertures where Cs effect was not saturated. The overall NI yield could have been influenced also by the presence of the PG mask on the downstream side of the plasma grid, which offers a surface equal to the closed apertures and is not temperature-controlled, resulting in an effective temperature presumably higher than the nominal one.

In the case of longer repetition time (low duty cycle), a detrimental effect on performances is found at room temperature (35 °C), indicating that the relatively higher sticking probability at this temperature, and the longer time between plasma discharges, combines in such a way that an optimal amount was exceeded. It is possible that the co-deposition of impurities, more probable at low temperatures, has also a cumulative effect during pauses between plasmas. Qualitatively speaking, in the balance of fluxes at the converter surfaces, sticking at 80°C during 2.5 mins provides an equilibrium condition that is not very different than the case of 100°C for 5.5 mins in terms of effectiveness. At lower temperatures, the stability of ion and electron currents during the beam pulse became poorer.

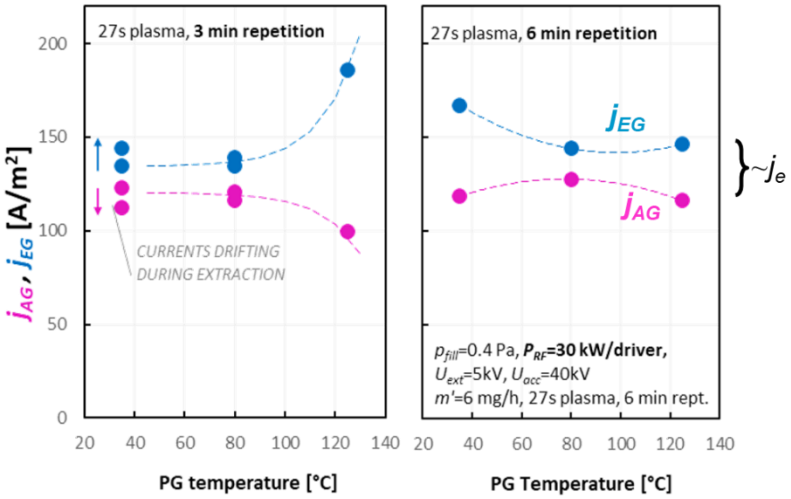

Figure 6 – Saturation values of I_{EG} and I_{AG} currents achieved for for identical source parameters, but with different plasma grid temperature. On the left, repetition time of 3 min; on the right hand side, repetition time of 6 min. The dashed

lines are just a guide for the eyes.

Investigation of multibeamlet operation and single-beamlet optics

In the SPIDER beam source, the accelerator electrodes feature multiple apertures, and the source plasma is generated by eight independent RF drivers; the operation shall aim at obtaining uniform beam parameters over the very large beam section. An example of optimised configuration for the operation at 4 kV extraction voltage is presented in Figure 7. The instrumented calorimeter STRIKE is at a distance of 0.5 m from the grounded grid, and the beamlet footprint width reported in the figure is obtained from bidimensional Gaussian fit of the temperature distribution on the rear side of the tiles. The current densities of the single beamlets are obtained subdividing the current collected at each of the instrumented tiles (each of the 16 tiles was biased at 60 V) among the beamlets, using the volume of the Gaussian fit. Normally, the beam current I_{beam} measured at STRIKE tiles is less than 0.85 times the accelerated current I_{AG} measured at the accelerator power supply. The bias currents were set to relatively low values (I^*_{bias} =80 A, I^*_{BP}=0 A) to improve the vertical uniformity of the beam profile, and the filter field was limited to 1.05 kA for achieving stable plasma discharge at low pressure, while minimising the co-extracted electron current. The available negative ion current density is different among the beamlets; however, thanks to the rather flat minima of beamlet divergence on the underperveance side with respect to the extraction voltage, the non-uniformities on the scale of the beamlet group can be dealt with. The optima presented in the figure were found by reducing to about 115 kW the total RF power, but balancing independently the four RF power generator. Due to the aforementioned limitation to the acceleration voltages, this study could not be repeated at higher current densities while preserving a good beamlet optics and full transmission of the accelerator.

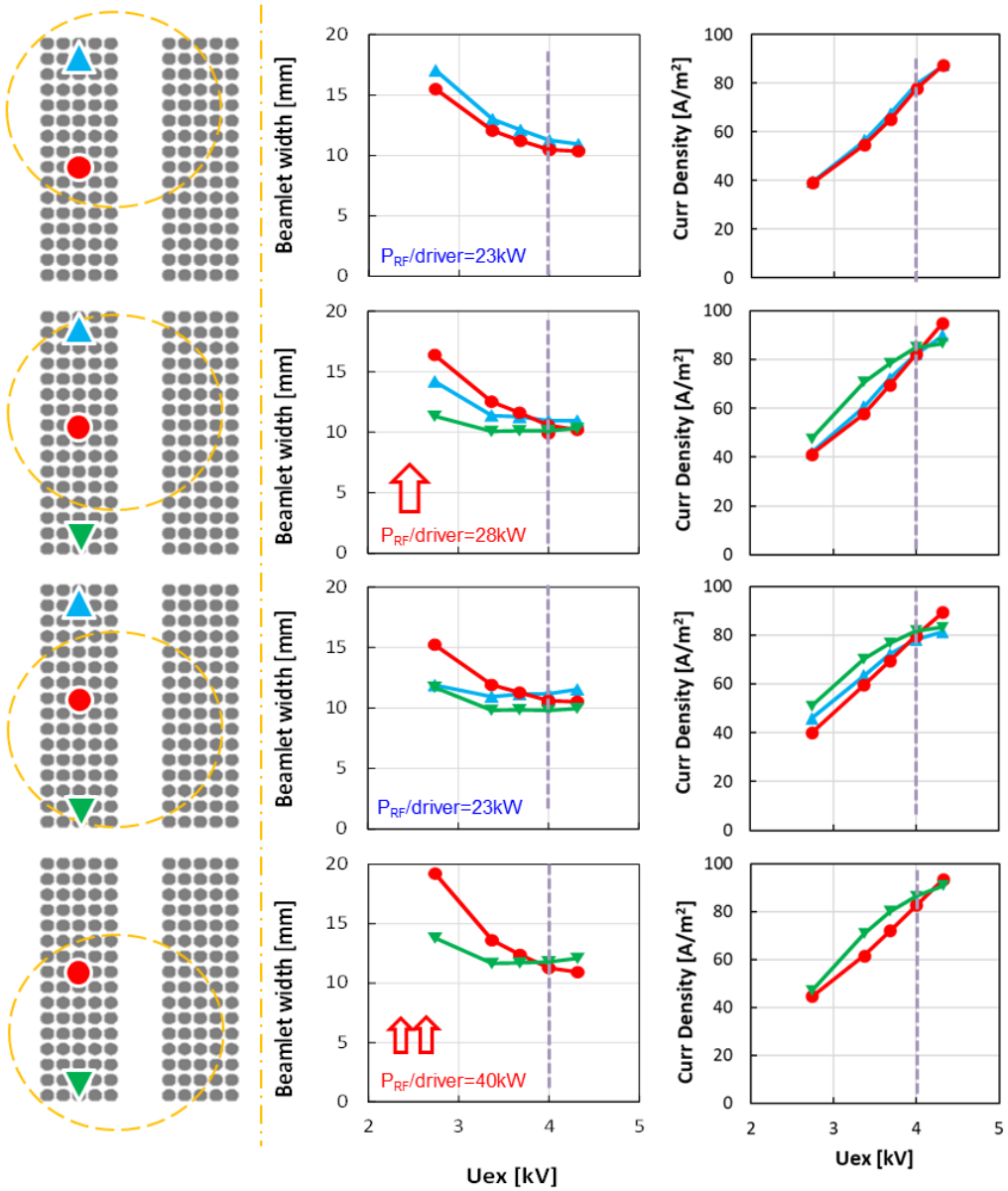

Figure 7 – Beamlet footprint width 1/e (STRIKE at 0.5m), and beamlet current density based on both two-dimensional

Gaussian fit and on the electric current collected at the instrumented calorimeter tiles ; U_{EG} scan in macropulse 9281 and 9282; U_{AG}/U_{EG}=9.5, p_{fill}~0.35 Pa, I_{PG}=1.05 kA (1.6 mT), 23 kW<P_{RF}/driver<40 kW, I^*_{bias} =80A, I^*_{BP}=0A, V_{bias}=29.9V, V_{BP}=26.2V, $j_e/j_{-,AG}$~1 @4 kV. The schematic on the left shows the beamlet position on the left half of the accelerator as seen from downstream the calorimeter; projection of driver positions are also highlighted.

The beam profile at higher RF power was studied only at very low U_{AG}/U_{EG} ratio: in this condition the transmission of the ion beam through the accelerator could be lower than one, especially in low-perveance cases. Figure 8(a) and 8(d) show the vertical profile of beamlet parameters (equivalent current density and e-fold width) for uniformly applied RF power of 50 kW/driver and extraction voltage of 7.5 kV; this ensures the extraction of the maximum available negative ion current (even at the beamlets with maximum available current density).

The beam seems to present vertical non-homogeneities, both on the source-scale (from top to bottom) and within a single segment. Concerning the latter scale, similar beam current profile within each grid segment was previously seen in volume operation [43], and a vertical profile of plasma density illuminating the grid segment was also measured previously with movable probes [44]. These effects appear to be mitigated by improving the caesium effect, which in our case is exemplified with the case of reduced PG temperature from 125°C to 80°C: when the Cs effect increases, underperveance beamlets improve their divergence, as they get closer to the best optics (Figure 8(b) and 8(e)). The overall uniformity of the vertical profile is also improved by increasing the Cs evaporation rate, as shown in Figure 8(c) and 8(f). These two effects are an indication that beam uniformity can be improved by building up a more resilient Cs layer. When a reduced extraction voltage U_{EG}=5.5 kV was applied in the attempt to limit the extracted ion current and develop a more uniform profile of accelerated current, the non-uniformity remains but in terms of beamlet divergence: the overperveant beamlet at the top conserves the effect of the higher available current density, so that the beamlet width is much larger than the others (shown by the dashed line in Figure 8 (b) and 8(e)). The same evidence is present in Figure 8 (f): when the Cs evaporation is increased, beamlets with higher accelerated current display increased divergence, indicating overperveance at the extraction and loss of negative ion current at the EG.

In this experimental setup with isolated apertures, it was possible to install current meters (LEM CTSR 0.3p) downstream the acceleration grid (grounded grid) for the measurement of the single beamlet current. In the presence of RF fields and magnetic fields produced by PG current, a cautionary correction was applied by subtracting the sensor voltage during steady state RF from the sensor voltage during beam acceleration [45]. Figure 8(a) presents the beamlet current density measured by the current meters installed downstream the grounded grid for comparison with the beam current estimated with the instrumented calorimeter STRIKE. Such measurement is very interesting for the study of the perveance of the extractor: the accelerated current density measured by current meters during an U_{EG} ramp is presented in Figure 9, for the same source parameters as in Figure 8(a). Around the knee of the Child-Langmuir plot or slightly after, the beamlet exhibits the minimum divergence according to STRIKE measurements. After the knee, the curve flattens; a limit of NI current density available at the meniscus is reached. However, even after saturation there is a small increase with increasing voltage, because of the increasing collection area when the meniscus is pushed back towards the plasma along the conical PG aperture. For the study of the caesium effect on the NI current, clearly the high-voltage region of these curves shall be considered, in order to avoid limiting the extracted current by space-charge; however, the choice of an appropriate U_{EG} to define the NI current is not easy to be defined, as U_{EG} should correspond to the best beamlet optics, but this cannot be achieved easily in multi-aperture accelerators. We should remark also that these current meters measure the accelerated beamlet current: this is an underestimation of the extracted current, both because of stripping losses and because a fraction of negative ion current could be intercepted by the acceleration grid if the single beamlet is far from perveance match. In addition to the issue of transmission loss at the acceleration grid, the Child-Langmuir plot also shows that for relatively low extraction voltages (i.e. in the space charge limited region), in the presence of a different availability of negative ions for extraction, the beamlet current follows a different curve. The transmitted current through the EG aperture (i.e. the quantity measured as accelerated beamlet current) is lower in the case of extra NI available at meniscus than in the case of limited NI ions, as can be seen by comparing the H1 to the H3 curve. Such interception by the EG occurs, because a higher current density implies meniscus pushed towards the EG and more diverging ion trajectories in the PG-EG gap. This behaviour is found consistently also using the same sensor and different RF power (not shown). The extractor perveance obtained by this measurement is indicated by the dashed line in Figure 9, however it should be noted that the presence of a 0.63 mm thick PG mask might affect the perveance.

The plot also indicates that the extraction voltage of 7.5 kV was sufficient in this case to achieve saturation of the negative ion current (i.e. departure of the current-voltage characteristics from Child-Langmuir limit) even at the beamlet with higher accelerated current density.

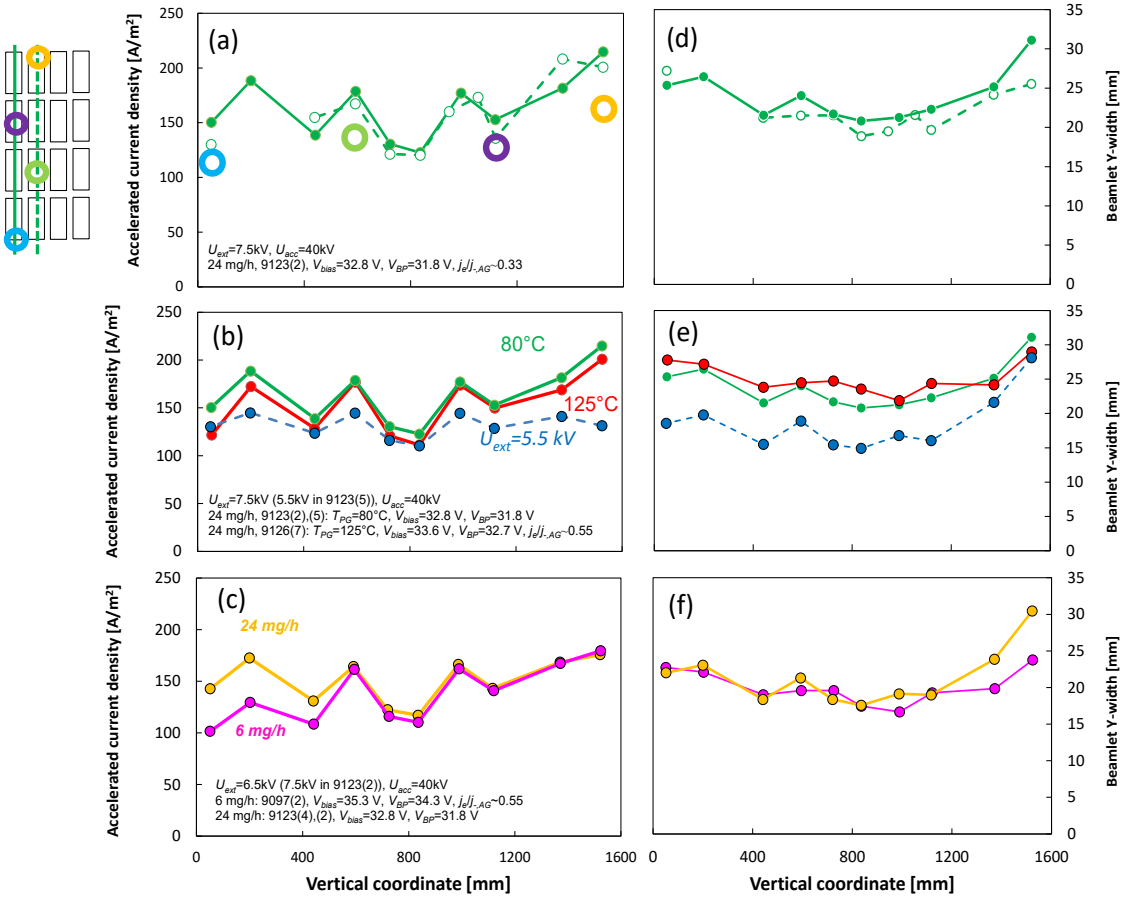

Figure 8 – On the left, vertical profile of accelerated current density of the single beamlets, calculated based on two-dimensional Gaussian fit, and on the total current on each of the instrumented calorimeter tiles biased at 60 V; On the right, single beamlet e-fold width on the rear side of STRIKE. (a) vertical profiles at two horizontal position, compared to saturation current density measured by current meters; (b) beam profile with two different PG temperatures (external profile) and with reduced extraction voltage; (c) beam profile measured with different evaporation rates (external profile); (d), (e), (f) beamlet width for the cases on the left; please note that the beamlet width is large because of the low U_{AG}/U_{EG} ratio that was possible to apply. RF power 50 kW/driver, I^*_{bias}=80A=I^*_{BP}.

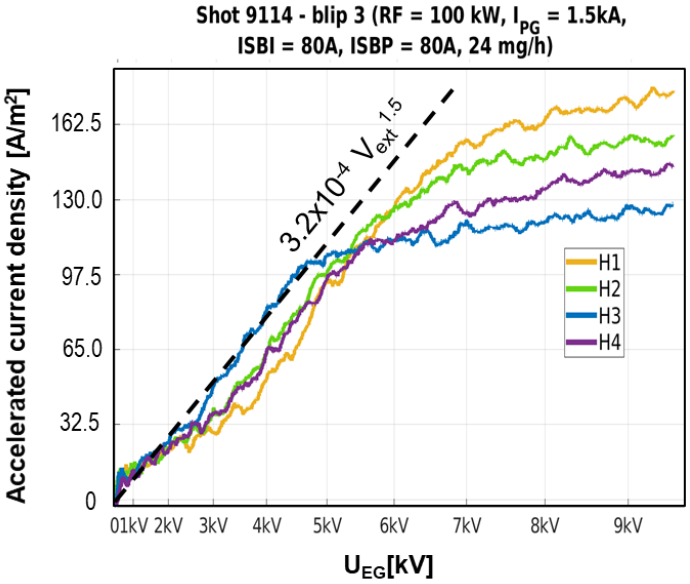

Figure 9 – Child Langmuir plot of the accelerated single-beamlet current measured at four beamlets, as a function of the applied extraction voltage to the power of 3/2 (the line color indicates the current meter position, following the color scheme in the inset of Figure 8); in pulse 9114(3), V_{bias}=33.2V, V_{BP}=32.3V.

The beam optics at high beam intensity was also studied by the Allison-type Emittance Scanner (AES) and the Beam Emission Spectroscopy (BES). Differently from other beam-intercepting diagnostics that provide the beam footprint, the AES provides the vertical beamlet emittance in y,y' space. It measures the current density at various vertical angles, while moving along a vertical profile. From the Doppler broadening of the H_α emission, the BES also measures the transverse velocity distribution of the beamlet particles, by knowing the angle of the line of sight with respect to the beamlet direction. In the present experimental setup, the AES and BES diagnostics can provide – for the same isolated beamlet – the angular distribution along the vertical and horizontal direction respectively.

Figure 10 presents the current density and divergence of one single beamlet, measured with different PG temperatures, at low RF power (23 kW/driver) and low filling pressure (about 0.33 Pa). For fixed source parameters but different PG temperatures, the data shows a clear decrease of available negative ion current above 80 °C (as discussed previously on the basis of average beam currents). The intensity of the beamlet emission from the BES signal (corrected for the beam energy and different intercepted fraction with varying divergence as described in appendix 1) indicates a trend similar to the AES.

The value of e-fold angular divergence ω is obtained from both diagnostics by fitting the angular distribution only above one tenth of the amplitude, with one single normal distribution. Even though this simple definition is not suitable for describing the non-Gaussian tails of the angular distribution, it still allows the analysis of the single-beamlet optics along vertical and horizontal directions, using results of two very different diagnostics.

The departure of the angular distribution from the reference distribution was calculated in terms of D-value of the Kolmogorov statistics, using AES data; for the purpose of our discussion, the D-value can be considered an indication of the beamlet current fraction not represented by the Gaussian distribution (i.e. proportional to a beam halo fraction at larger angles). The indicator never exceeded 9% for the presented cases; however, as reported in the histogram shown in Figure 10, the single Gaussian approximation appears to best suit the data at low extraction voltages – a condition in which beamlet scraping by the EG aperture is also possible, so that the broad divergence component is removed from the accelerated beam. It should be noted that, using the whole emittance to calculate the *rms* divergence, the minimum e-fold angular divergence would be never lower than 13 mrad. The signal-to-noise ratio did not allow a similar quantitative estimation using the BES spectra (as the line of sight was intercepting one single beamlet, at relatively low current and energy).

The divergence angle calculated as previously described is larger along the horizontal direction (measured by BES) than along the vertical one (measured by AES). This difference could be due to the geometry of the PG mask apertures [35], or to the presence of electron deflection magnets in the EG and AG: indeed, their vertical magnetic fields deflect ions horizontally during acceleration, causing beamlets to enter the electrostatic lenses with an horizontal offset; as a consequence, second-order effects cause the ion velocities to spread horizontally [45]. This was seen previously in Cs free operation, with a much greater differentiation among vertical and horizontal directions (co-extracted electrons might amplify the difference) [22].

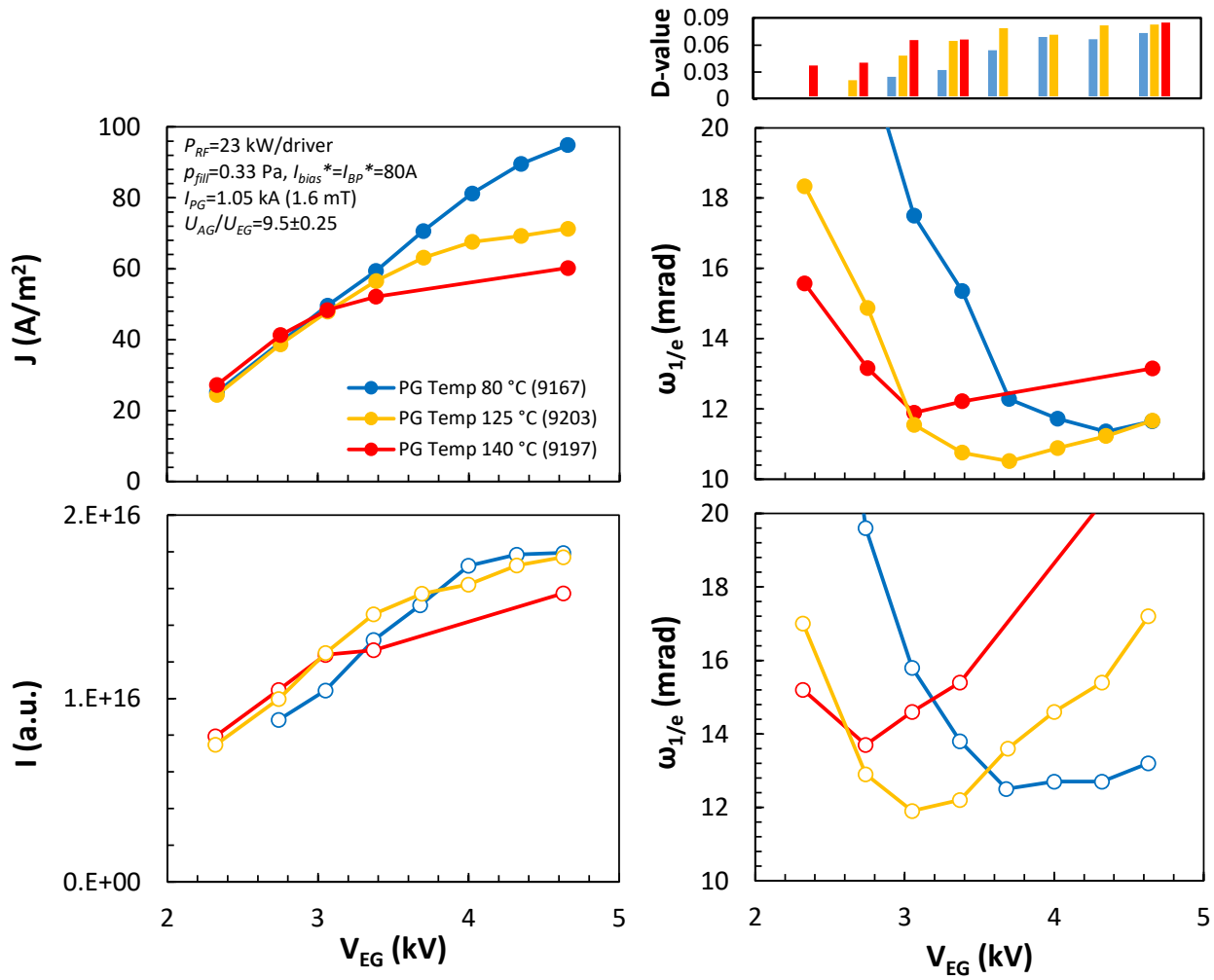

Figure 10 – On the left, estimation of single-beamlet current; on the right, estimation of *e*-fold angular divergence; on top, data from Allison-type emittance scanner (AES); at the bottom, data from beam emission spectroscopy (BES). Estimated error bar of AES angular resolution not better than 0.7 mrad. U_{EG} scan during macropulses 9167, 9203, 9197; V_{bias} respectively 30.2 V, 29.8 V, 30.3 V; V_{BP} respectively 29.4 V, 29.2 V, 29.6 V; $j_e/j_{-,AG}$~0.1, 0.55, 1.2 @4 kV.

Beam stability in deuterium

For deuterium ions, the threshold of impact energy for Cs sputtering is smaller than in the case of hydrogen (see [19] and references therein), so that the equilibrium of caesium coverage at the converter surfaces is expected to change. The use of a mask covering most apertures ensures the possibility to compensate, using relatively large Cs evaporation rates, while minimising the risk of voltage holding issues at the extractor. For this first operation of SPIDER with deuterium in surface production, we operated at 50 kW/driver and used 48 mg/h total evaporation rate with no indications of overcaesiation (i.e. increased breakdown probability at the extractor or reduction of plasma light from RF drivers). Figure 11 reports the stability of the beam current and of the extraction power supply currents for the hydrogen and deuterium beam, presented in terms of beam current, as measured by the instrumented calorimeter STRIKE. The extraction voltage (7~7.5 kV) is high enough so as not to fall in the space-charge limit region within the extractor, according to Child-Langmuir plots obtained by current meters during the same experimental session. With similar source parameters and extraction voltages, when compared to the case of hydrogen the time trace of beam current in deuterium was stable and the co-extracted electron current showed a slight decrease. The extracted current density is of the order of 115 A/m^2, with isotope mass affecting the ion current as expected from results of ELISE source [48]. The relatively high electron current (electron-to-ion ratio of about 4) is mainly due to the choice of a low filter-field of 2.4 mT, a compromise to maximise the beam uniformity by minimising vertical drifts. Despite the limited experimental time dedicated to the study of isotope effect, this early result in deuterium confirmed the issues already found in RF and arc sources concerning the co-extracted electron current. Also in the case of the full-size ITER NBI source, we found a clear indication that the best source parameters found in hydrogen can be different than those required for deuterium, and will require a dedicated optimisation.

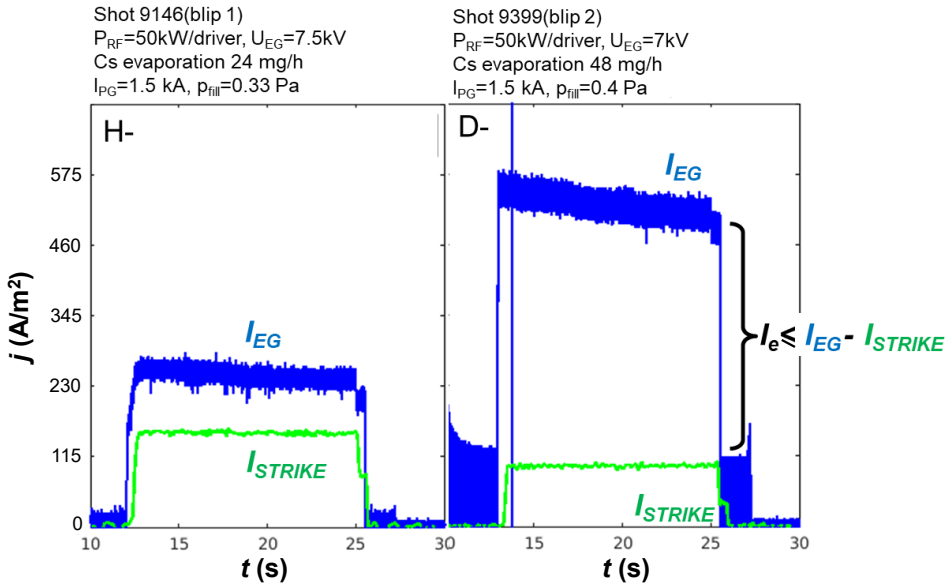

Figure 11 – examples of beam stability during hydrogen and deuterium beam acceleration. In 9146(1), I^*_{bias}=80A=I^*_{BP}, V_{bias}=33.5V, V_{BP}=32.4V; in 9399(2), I^*_{bias}=190A, I^*_{BP}=80A, , V_{bias}=35.7V, V_{BP}=33.5V;

Summary and conclusions

The caesium conditioning of the full-size ITER NBI prototype source SPIDER was performed for the first time. The experimentation covered technical aspects, related to the commissioning and first operation of the caesium ovens, caesium diagnostics, and the gradual increase of high voltage acceleration. It also covered the investigations of caesiation procedure in SPIDER, and of the source performances in terms of extracted negative-ion current density and co-extracted electrons, in the present configuration with limited number of extraction apertures. In this regard, the source performances in the five phases of the campaign are summarised in Figure 12: at the top, the initial phases of the caesiation at various RF power are presented; at the bottom, all phases are overlapped; on the left hand side, the average current density of the negative ion beamlet estimated from the drain current measured at the acceleration power supply is shown, while on the right hand side the plots present both the negative ion current density and the electron-to-ion ratio as estimated from the current collected at the instrumented calorimeter STRIKE.

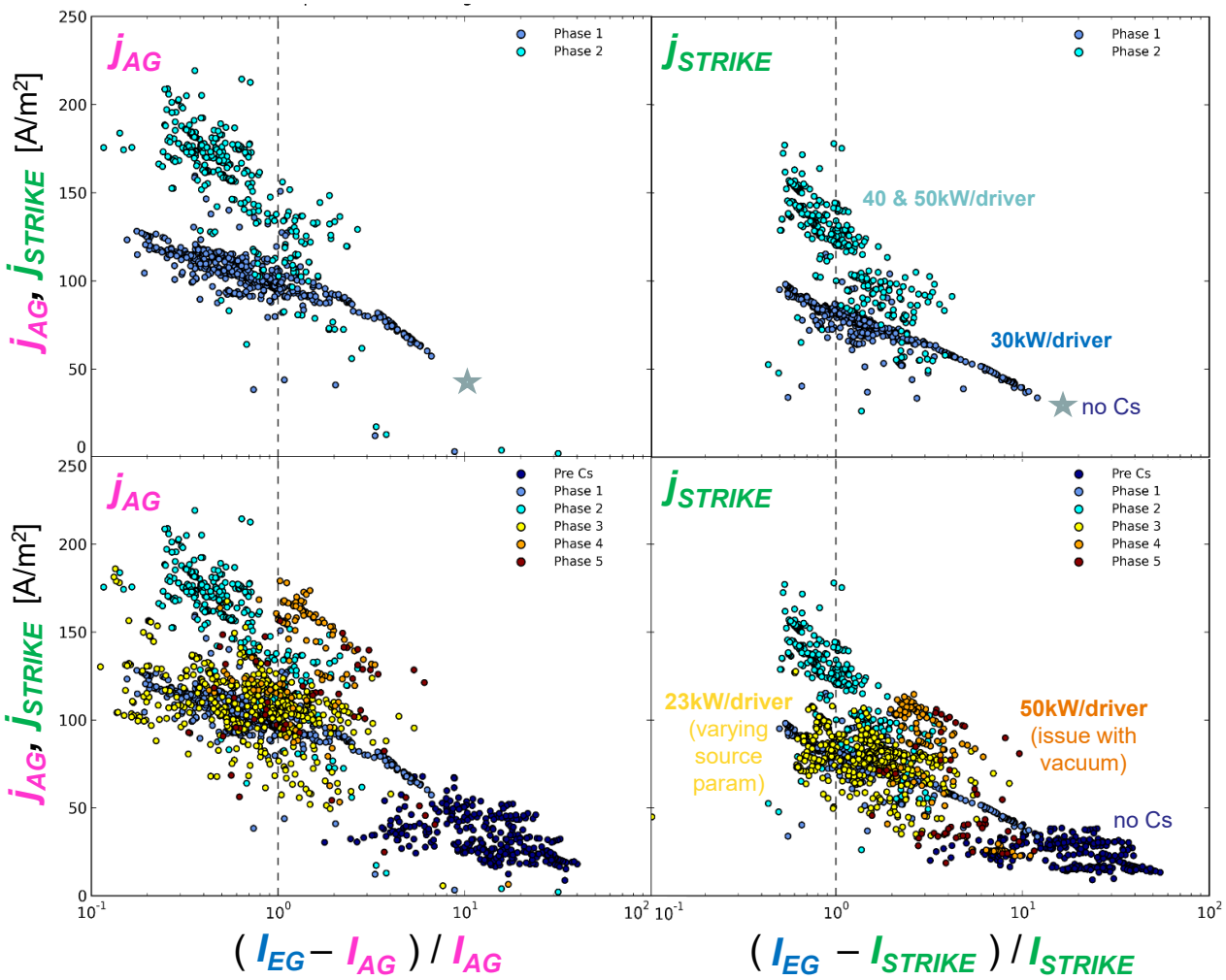

Figure 12 – performance plots of the various phases of the first caesium campaign in SPIDER, showing the accelerated current density or beam current density versus a ratio proportional to the ratio of co-extracted electrons and negative ions. Points are time-averaged quantities during beam extraction.

In the present operating conditions for SPIDER (as detailed in section 2), the first campaign with caesium has highlighted the following aspects:

- in pulsed operation, higher Cs injection has the same role as longer pause between plasma pulses. The plasma duration has a detrimental effect on the Cs effectiveness;
- in the present conditions, a PG temperature of 80 °C was found to maximize the NI beam current in the explored range (35 °C<T_{PG}<125 °C);
- the role of PG and BP bias is slightly different at different RF power and filter field; however, it is generally found that increasing I_{bias} is more effective than I_{BP} in improving the electron to ion ratio at the extraction, both at low or and high RF power;
- on the scale of the whole source, the beam profile can be uneven; nevertheless, a non-uniformity on the scale of the beam segment could be corrected by tuning the RF power of the four independent RF generators, while keeping other source parameters such as filter field and biases constant. Both the filter field and biases actually modify the vertical profiles, although their effect can be different depending on the RF power;
- on the scale of the single grid segment, the vertical beam profile has a non-uniformity that might be correlated to non-uniformities of the plasma illuminating the PG within the frame of the bias plate apertures, which depends itself on the discrete structure of the multi-driver RF sources; for a fixed filter field strength, the non-uniformity was marginally improved by caesiation and was influenced by the relative bias of plasma grid and bias plate;
- the minimal angular divergence at 0.3 Pa measured by the emittance scanner was ~12 mrad at low RF power and beam energy of 37 keV; it decreases lower at higher pressure, with minor effects from bias currents and filter field. The measurement was performed at optimal perveance, requiring the reduction of RF power to 23 kW/driver in order to accommodate the present limit of acceleration voltage (about 45-50 kV);
- no meaningful increase of the frequency of accelerator breakdowns, ascribable to excessive caesium evaporation,

was found with respect to caesium-free operations; in the next SPIDER experimentation, with longer experimental time and longer caesium injection, this condition will be verified.

Further observations, which are more specific of the SPIDER experiment in the present state, are related to the effect of performing complete cryopump regeneration without isolating the caesiated plasma source. In the rather poor vacuum conditions of SPIDER, performing the total regeneration in the last days of the campaign after the relatively large leak appeared, did not deteriorate the caesium effect: on the contrary, the NI current was restored back to the values of the first weeks of experimentation.

Despite the present limits of the accessory plants, in particular of the vacuum system, the outcome of the SPIDER experimentation is of the utmost importance for preparing the initial operation of MITICA, the full-scale prototype of ITER NBI, in particular for minimising the risks in planning the early caesium operations. Indeed, the presented results were obtained for the first time in a negative ion source of the same size and of identical design as that of ITER NBI. A most urgent challenge is now to address the present limitations of the SPIDER facility, so as to extract and optimise the full beam of 1280 apertures also during long pulses of up to 1000s in hydrogen. These will be the main topics of research in SPIDER to support the beginning of caesium operation in MITICA, planned for 2025-2026.

Acknowledgements

This work has been carried out within the framework of the ITER-RFX Neutral Beam Testing Facility (NBTF) Agreement and has received funding from the ITER Organization. The views and opinions expressed herein do not necessarily reflect those of the ITER Organization. This work has been carried out within the framework of the EUROfusion Consortium, funded by the European Union via the Euratom Research and Training Programme (Grant Agreement No 101052200 - EUROfusion). Views and opinions expressed are however those of the author(s) only and do not necessarily reflect those of the European Union or the European Commission. Neither the European Union nor the European Commission can be held responsible for them.

Appendix 1

In a symmetric Gaussian approximation of angular distribution, the beamlet is composed by laminar ion trajectories and the velocity components v_x, v_y perpendicular to the beamlet axis z reads

$$v_x(x) = v_z A\{\exp(-x^2/\omega_{xy}^2)\}, v_y(y) = v_z A\{\exp(-y^2/\omega_{xy}^2)\} \quad \text{eq. 3}$$

with A being a normalization constant and ω_{xy} the 1/e width of the distribution. The beamlet density in x, y space can be derived at any distance L from the grounded grid of the accelerator, when a focal length f is assumed (with respect to the grounded grid itself, normally $f < 0$), so that the density of the beamlet along the radial direction is itself Gaussian and only depends on the e-fold angular divergence ω:

$$\omega_{xy} = \omega(L - f) \quad \text{eq. 4}$$

More refined approximations could be used to describe the beamlet in the phase-space, but this simple treatment is sufficient for the purpose of this appendix. Independently from the specific photon collection probability (which depends on the angle of the lines of sight in the experimental setup) the photon emission of particles within the quasi-cylindrical line of sight of beam emission spectroscopy is

$$I = \frac{1}{4\pi}\int_{C,\Sigma} n_b n_T \sigma v_z dV d\Sigma \approx \frac{\Sigma}{4\pi}\iiint_C n_b n_T \sigma v_z dV \quad \text{eq. 5}$$

with n_b and $v_z$the beam density and axial velocity respectively, n_T the gas target density, and σ the cross-section for electronic excitation and subsequent H_α emission (namely, the cross section for electron detachment of the fast negative hydrogen ion). The integration volume C describes the LOS cylinder. Σ is the integration over the solid angle from which the optical head is seen from any position within C; given the distance from the beamlet, we can assume uniform Σ for all particles (in the order of 1.25×10^{-5} sr).

The beamlet current is proportional to the beam particle density, so that from the definition of current,

$$I_b = \frac{1}{\Delta t}\int_{x=-\infty}^{\infty}\int_{y=-\infty}^{\infty}\int_{z=-v_z\Delta t}^{0} q n_b dV \quad \text{eq. 6}$$

the beamlet current I_b is proportional to the number of particles within a slab of length v_z.

The ratio between the the beamlet current I_b and the intensity I is therefore

$$\frac{I_b}{I} = \frac{\frac{1}{\Delta t}\int_{x=-\infty}^{\infty}\int_{y=-\infty}^{\infty}\int_{z=-v_z\Delta t}^{0} q n_b dV}{\frac{\Sigma}{4\pi}\iiint_C n_b n_T \sigma v_z dV} \approx \frac{4\pi q}{\Sigma n_T \sigma v_z}\frac{v_z}{d}\frac{\int_{x=-\infty}^{\infty}\int_{y=-\infty}^{\infty}\int_{z=-d}^{0} n_b dV}{\iiint_C n_b dV} = \frac{1}{\sigma}\frac{N_{slab}}{N_{cyl}}\cdot\frac{4\pi q}{\Sigma n_T d} \qquad \text{eq. 7}$$

in which the LOS diameter $d = v_z\Delta t$ was chosen as width for the calculation of the number of beam particles N_{slab}, while the number of particles within the cylinder is N_{cyl}.

When the beam energy is changed, both the cross section σ and the beam divergence ω are modified, and the intensity of the BES signal collected for different beam parameters might not vary proportional to the beamlet current. In relative terms, since the slab width was conveniently chosen to be constant, the total beamlet current is proportional to a corrected intensity I', which can be obtained form the measured intensities by considering only two correction parameters, one depending on the energy (cross-section) and the other depending on the divergence (i.e. the ratio of integrals):

$$I_b(\omega, E) \propto I' = \left(\frac{1}{\sigma(E)}\cdot\frac{N_{slab}}{N_{cyl}(\omega)}\right)\cdot I \qquad \text{eq. 8}$$

The correction factor N_{slab}/N_{cyl} as a function of beam divergence ω, calculated with Monte Carlo approach, are reported in the following Figure 13, while for the correction related to the cross-section we refer to any database [49]. As examples, the cases of non-ideal alignment and different equivalent beamlet radius at the grounded grid are presented. It should be noted that the correction depends mainly on the divergence along a direction perpendicular to the line of sight and the beamlet axis, which might be different from the other component of divergence which can be measured by the diagnostic.

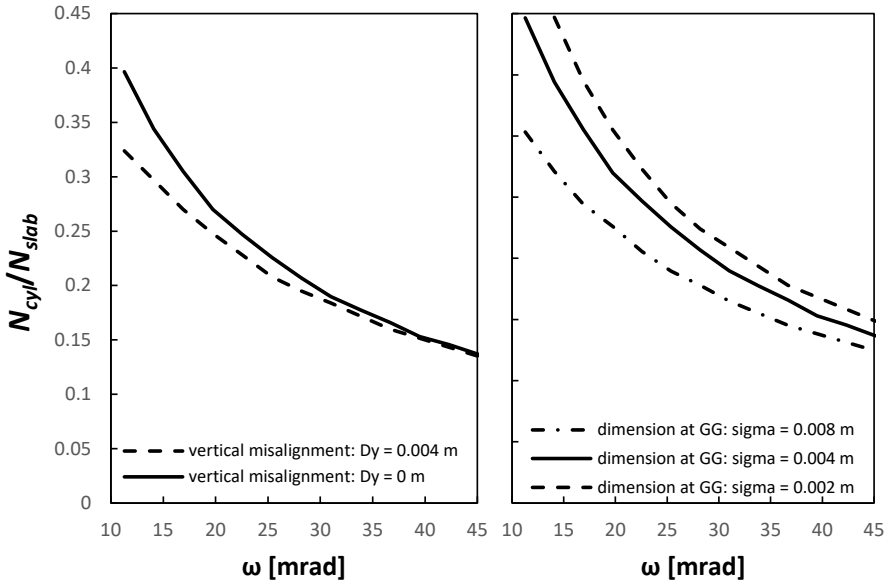

Figure 13 – On the left, dependence of intercepted fraction with vertical offset of the line of sight (sigma radius at GG 4 mm); on the right, dependence on assumed radius at GG (for ideal axial alignment of beamlet axis and line of sight).

References

1. L.R. Grisham, et al., Fusion Engineering and Design 87 (11), 1805-1815 (2012) https://doi.org/10.1016/j.fusengdes.2012.08.001
2. R S Hemsworth, et al., New J. Phys. 19 025005 (2017) https://doi.org/10.1088/1367-2630/19/2/025005
3. E. Speth, et al., Nucl. Fusion 46 S220 (2006) https://doi.org/10.1088/0029-5515/46/6/S03
4. B. Heinemann, et al., Fus. Eng. Design 86 (6–8) 768-771 (2011) https://doi.org/10.1016/j.fusengdes.2010.11.031
5. B. Heinemann, et al., New J. Phys. 19 015001 (2017) https://doi.org/10.1088/1367-2630/aa520c
6. G Serianni, et al., Fus Eng Design 146, 2539-2546 (2019) https://doi.org/10.1016/j.fusengdes.2019.04.036
7. G. Serianni, et al., Review of Scientific Instruments 91 (2), 023510 (2020) https://doi.org/10.1063/1.5133076
8. V. Toigo, et al., Nucl. Fusion 59 086058 (2019) https://doi.org/10.1088/1741-4326/ab2271

9. Y.I. Belchenko, G.I. Dimov, V.G. Dudnikov, Nucl. Fusion 14 p. 113-114 (1974) https://doi.org/10.1088/0029-5515/14/1/017
10. M. Bacal, M. Wada, Applied Physics Reviews 2, 021305 (2015); https://doi.org/10.1063/1.4921298
11. J. Hiratsuka, et al., Review of Scientific Instruments 91, 023506 (2020); https://doi.org/10.1063/1.5131302
12. R. Friedl, U. Fantz, Journal of Applied Physics 122, 083304 (2017); https://doi.org/10.1063/1.5000373
13. A. Kojima, et al., Nucl. Fusion 51 083049 (2011) https://doi.org/10.1088/0029-5515/51/8/083049
14. D Wunderlich, et al., Plasma Sources Sci. Technol. 18 045031 (2009)
15. R McAdams, et al., Plasma Sources Sci. Technol. 20 035023 (2011)
16. A. Rizzolo, et al., Fusion Engineering and Design 88 (6–8) p. 1007-1010 (2013) https://doi.org/10.1016/j.fusengdes.2013.02.099
17. R. Gutser, et al., Plasma Phys. Control. Fusion 53 105014 (2011) https://doi.org/10.1088/0741-3335/53/10/105014
18. HPL De Esch, et al., Nuclear Fusion 55 (9), 096001 (2015) https://doi.org/10.1088/0029-5515/55/9/096001
19. N Marconato, et al., Fus. Eng. and Des. 166 112281 (2021) https://doi.org/10.1016/j.fusengdes.2021.112281
20. P. Agostinetti, et al., Nucl. Fusion 51 063004 (2011) https://doi.org/10.1088/0029-5515/51/6/063004
21. R. Pasqualotto, et al., JINST **12** C10009, https://doi.org/10.1088/1748-0221/12/10/C10009
22. A. Pimazzoni, et al., Rev. Sci. Instrum. 91, 033301 (2020); https://doi.org/10.1063/1.5128562
23. M Barbisan, et al., Plasma Phys. Control. Fusion 63 125009 (2021)
24. C. Poggi, et al., Fus. Eng. And Des. **168** 112659 (2021) https://doi.org/10.1016/j.fusengdes.2021.112659
25. M Spolaore, et al., J. Phys. D: Appl. Phys. 43 124018 (2010) https://doi.org/10.1088/0022-3727/43/12/124018
26. B. Zaniol, et al., Rev. Sci. Instrum. 91, 013103 (2020); https://doi.org/10.1063/1.5128900
27. M Barbisan, et al., Plasma Phys. Control. Fusion 64 065004 (2022), https://doi.org/10.1088/1361-6587/ac65b0
28. M. Barbisan, et al., JINST, 14 C12011 (2019) https://doi.org/10.1088/1748-0221/14/12/C12011
29. E. Sartori, IEEE Trans Instrum Meas 69 (7), 4975-4986 (2020) https://doi.org/10.1109/TIM.2019.2955773
30. M. Hanada, et al., Review of Scientific Instruments 61, 499 (1990); https://doi.org/10.1063/1.1141233
31. N Marconato, et al., Numerical and experimental assessment of the new magnetic field configuration in SPIDER, IEEE Trans Plasma Science (2022), https://doi.org/10.1109/TPS.2022.3167859
32. V. Candeloro, et al., Electron scraping and electron temperature reduction by bias electrode at the extraction region of a large negative ion source, accepted for publication in IEEE Transactions on Plasma Science
33. A. Zamengo, et al., Fusion Engineering and Design 173 (2021) 112790
34. A. Maistrello, et al., Fus Eng Design, 167, 112337 (2021); https://doi.org/10.1016/j.fusengdes.2021.112337
35. M. Pavei, et al., Fus Eng Design 161, 112036 (2020) https://doi.org/10.1016/j.fusengdes.2020.112036
36. H. Nakano et al JINST 11 C03018 (2016) https://doi.org/10.1088/1748-0221/11/03/C03018
37. A. Rizzolo, et al., Fus. Eng. Des. 146(A) p. 676-679 (2019) https://doi.org/10.1016/j.fusengdes.2019.01.053
38. M. De Muri, et al., Fusion Engineering and Design 167, 112331 (2021) https://doi.org/10.1016/j.fusengdes.2021.112331
39. E. Sartori, et al., AIP Conference Proceedings 2052, 040011 (2018) https://doi.org/10.1063/1.5083745
40. *M. Bigi, et al., "Early operational experience and improvements of SPIDER ion source power supplies at beam energies exceeding 30 keV" presented 29th IEEE Symposium on Fusion Engineering (SOFE) conference 2021, submitted IEEE Trans Plasma Science*
41. F. Gasparini, M. Recchia, M.Bigi, T. Patton, A. Zamengo, E. Gaio., Fusion Eng. Des. 146 (2019) 2172–2175
42. M Fadone, et al., Review of Scientific Instruments 91 (1), 013332 (2020) https://doi.org/10.1063/1.5129666
43. A Pimazzoni, et al., Fus Eng Design 168, 112440 (2021) https://doi.org/10.1016/j.fusengdes.2021.112440
44. E. Sartori, et al, Fus Eng Design 169, 112424 (2021) https://doi.org/10.1016/j.fusengdes.2021.112424
45. *A. Shepherd et al, "Initial Results from the SPIDER Beamlet Current Diagnostic," presented 29th IEEE Symposium on Fusion Engineering (SOFE) conference 2021, submitted Trans Plasma Science*
46. P Veltri, et al., Nuclear Fusion 57 (1), 016025 (2016) https://doi.org/10.1088/0029-5515/57/1/016025
47. E Sartori, et al., AIP Conference Proceedings 2052, 020006 (2018); https://doi.org/10.1063/1.5083724
48. D. Wunderlich, et al., Review of Scientific Instruments 90, 113304 (2019); https://doi.org/10.1063/1.5127832
49. C. F. Barnett et al., Atomic Data for Fusion, ORNL-6086 (1990)